JMEPEG (2021) 30:9118–9129
https://doi.org/10.1007/s11665-021-06104-5

1059-9495/$19.00

Experimental Investigation of Lattice Deformation Behavior in S355 Steel Weldments Using Neutron Diffraction Technique

Romali Biswal, Ali Mehmanparast, Supriyo Ganguly, and Joe Kelleher

Submitted: 28 March 2021 / Revised: 22 June 2021 / Accepted: 7 July 2021 / Published online: 19 August 2021

This study aims to investigate the influence of welding process on the elastic lattice deformation and its effects on fatigue and fracture behavior of S355 G10+M steel, which is widely used in fabrication of offshore wind turbine monopile structures. In situ neutron diffraction measurements were taken on cross-weld test samples at room temperature to monitor the evolution of intergranular strains under static and cyclic loading conditions. Both static and cyclic test results have shown that the {200} orientation exhibits the least load carrying capacity while {211} had the maximum stiffness. The hkl-specific response predicted using Reuss and Kröner model were found to agree well with experimental values obtained for the heat-affected zone for all the orientations; however, discrepancies between the experimental and model predictions have been observed for the base metal and weld metal. Moreover, the microstructural differences between the weld metal and heat-affected zone resulted in the maximum elastic–plastic strain mismatch at the interface of the two regions. The results from this experiment would be useful to understand the role of crystal-specific microstrains and lattice deformation on fatigue and fracture behavior of thick-walled monopile weldments.

Keywords elastic properties, life cycle assessment, neutron scattering, stress/strain relationship, welding

1. Introduction

With the growing demand of energy consumption around the globe, offshore wind energy has emerged as a sustainable source of renewable energy and received a lot of attention in recent years. Continued efforts are being made in all the different technical areas toward making the wind turbine technology more efficient and commercially as lucrative as the oil and gas industry (Ref 1, 2). The published literature indicates that the present standards (Ref 3) that are implemented for the design of wind turbine support structures, especially the monopile type foundation, are overly conservative (Ref 4-6). This leads to a substantial increase in the capital cost and added difficulty in terms of manufacturing and material handling. Moreover, a large number of weldments are employed in fabrication of offshore wind turbine (OWT) monopile foundations which require careful consideration in structural integrity and life assessment processes.

It is known that welding operation gives rise to heterogenous/graded structure in a welded component and introduces residual stresses which would significantly affect fatigue and fracture behavior (Ref 7). Inhomogeneous expansion under compressive plastic straining and contraction of the weld and associated heat-affected region leads to a variably distributed residual stress field which is tensile in and around the weld region, balanced by a compressive stress field further out in the parent metal (Ref 7). Such residual stresses can be either macroscopic in scale (type I), ranging up to several millimeteres, or microscopic in scale, with dimensions comparable to the grain size of the material. The residual stresses ranging in the microscopic scale can be intergranular (type II) or intragranular (type III) in nature (Ref 8). Welding of thick sections accumulate complex residual stress distribution due to

Abbreviations

v	Poisson's ratio
d	Atomic spacing
hkl	Miller Indices
bcc	Body-centered cubic
bct	Body-centered tetragonal
E	Young's Modulus
fcc	Face-centered cubic
BM	Base Metal
DIC	Digital Image Correlation
DNV	Det Norske Veritas
EBSD	Electron Backscatter Diffraction
FCG	Fatigue Crack Growth
HAZ	Heat-Affected Zone
OWT	Offshore Wind Turbine
SEM	Scanning Electron Microscope
WM	Weld Metal

Romali Biswal and **Ali Mehmanparast**, Renewable Energy Systems Centre, Cranfield University, Cranfield MK43 0Al, United Kingdom; **Supriyo Ganguly**, Welding Engineering and Laser Processing Centre, Cranfield University, Cranfield MK43 0AL, United Kingdom; and **Joe Kelleher**, ISIS-STFC Rutherford Appleton Laboratory, Didcot OX11 0QX, United Kingdom. Contact e-mail: a.mehmanparast@cranfield.ac.uk.

repeated thermal cycling from multiple passes. Additionally, the effect of differential plastic deformation due to texture variations result in the weldments to become preferred sites for crack initiation during application of load (Ref 9-11). Also, the mechanical response of a polycrystalline material is influenced by the microstructural parameters such as grain size, shape and orientation distribution, which are strongly affected by the welding operation (Ref 4, 12-14). The relatively fast transient thermal cycles applied during welding process lead to microstructural variations between the fusion zone or weld metal (WM), heat-affected zone (HAZ) and the base metal (BM). The application of cyclic loading is of particular interest since tensile residual stresses raise the mean stress and accelerate fatigue damage [15]. Therefore, it is important to develop a robust understanding on the effect of residual stress distribution on the structural integrity of welded joints, particularly for wind turbine applications where the weldments involve thick sections ranging between 30 and 125 mm [5] and are subjected to severe cyclic loading conditions due to constant exertion of wind and wave loads (in case of offshore wind turbines).

Residual stress measurement can be taken using a number of techniques that can be nondestructive, semi-destructive or destructive. Currently, diffraction-based methods are increasingly implemented owing to the advances in neutron sources, that use the atomic lattice planes as a gauge to monitor the strain response of a material and subsequently determine the three dimensional residual stress magnitude and distribution (Ref 6, 7). However, the variation in packing fraction of atoms along different crystallographic planes usually results in distinctly different (elastic and plastic) deformation behavior in microscopic length scale (Ref 16). In other words, the elastic constant and yielding depends on the atomic spacing, which changes with the crystallographic orientation of the grain with respect to the direction of applied load (Ref 17). In a recent work performed by Jacob et al. (Ref 6) the authors used neutron diffraction technique and finite element modeling to study the effects of residual stresses on the fatigue crack growth (FCG) behavior of S355 circumferential weld joint. It was observed that the FCG rate was increased almost by a factor of two when the crack tip was oriented such that the FCG direction and weld center line were at 0° angle as compared to the orientation where the FCG direction and weld center line were at 180°, with respect to the weld geometry (i.e., location of the crack tip with respect to the inner surface of the OWT monopile weldment). The reason for this behavior stems from the variation in the (type I) residual stress field at the weld joint that was reported to vary between 400 and − 400 MPa in the transverse direction (Ref 6), i.e., along the thickness of the weldment. In another study (Ref 14), a validated two-dimensional finite element model was used to conduct a parametric investigation on S355 weld joints (H-sections). It was revealed that the (type I) residual stresses at the junction were close to the yield strength of the material, thereby making such weld geometries prone to fatigue crack initiation.

Neutron diffraction is an advanced nondestructive technique that can be used to monitor spatially resolved stress distribution pattern (Ref 8), phase specific stresses(Ref 18, 19) and intergranular stresses (Ref 20) in the material volume. Furthermore, in situ neutron diffraction reveals the microplasticity associated with lattice orientation of constituting grain families (i.e., families of crystallographic planes) and phases as the material undergoes deformation. Mamun et al. (Ref 21) analyzed the effect of cyclic loading on grain length-scale deformations of 316 H austenitic steel using *in situ* neutron diffraction technique and reported the creep performance of the material with respect to prior loading history. The in situ neutron measurements were conducted over {200}, {220} and {311} grain families and the macroscopic stress and the lattice strain exhibited different values of elastic constants, hence indicating material anisotropy. Similar studies on in situ neutron diffraction with mechanical loading have been reported on stainless steel alloys such as 316 H (Ref 7, 22), duplex steel (Ref 8, 23), bearing steel (Ref 16) and pearlitic steel (Ref 24, 25). In (Ref 7), 316 H austenitic steel was found to exhibit higher local strain in {200} grain family and concluded that the failure was controlled by the accumulated equivalent plastic strain. Furthermore, according to (Ref 22), the onset of yielding in 316 H was reported to vary significantly between {200} and {220} grain families. Another study on duplex stainless steel reported mismatch between the elastic stresses induced in the ferritic and austenitic phases, such that higher stresses accumulated in the austenitic phase and the mismatch increased with an increase in the number of weld passes (Ref 8). Woo et al. (Ref 23) studied the uniaxial tensile failure of a duplex steel and concluded that necking is likely to initiate at sites with higher volume fraction of body-centered cubic (bcc) ferrite and body-centered tetragonal (bct) martensite phases. These studies provide evidence for the scope of enhancement of fatigue and fracture performance through texture alteration.

The fatigue response of structural steel has been studied by a number of researchers; however, there is limited research on cross-weld specimens, and the existing literature (Ref 6, 10-12) predominantly reports the FCG behavior in air and seawater conditions. While the studies on FCG behavior help in designing for a damage tolerant design approach, it is also important to understand how lattice orientation impacts the straining pattern in front of a crack tip and thereby the fatigue crack growth rate. In other words, for identical loading, how the response of BM, HAZ and WM would vary due to the crystal orientation distribution. To the best of the authors' knowledge, there is no research published on the effect of static and cyclic load on lattice deformation behavior of a smooth cross-weld specimen. Therefore, the present study aims to investigate the elastic and plastic straining pattern between: (a) the BM, HAZ and fusion zone, and (b) the difference in strain accumulation between different grain families in S355 G10+M steel grade which is frequently used for structural applications in OWT. Such finding could be useful in supplementing the material design data and improving the structural integrity of the component by interpreting the texture toward reducing the differential straining patterns. This data are also useful for developing prediction models that capture the microstructural interactions for structural steels and improve the reliability of the existing models used for optimizing the OWT designs.

2. Experimental Details

2.1 Material Selection

The experimental investigation was focused on structural steel grade S355 G10+M, which is predominantly used in fabrication of OWT foundations (Ref 11). Details of the chemical composition of the base metal and the filler wire

can be found in Table 1 (Ref 12). It should be mentioned that the monopile structure consists of two types of welds depending on the alignment of the weld with respect to the axis of the monopile, namely, longitudinal and circumferential weld (Fig. 1a). This study focuses on the circumferential weld only, where the weld axis is aligned parallel to the rolling direction of the plate. In the real application, thick sections are in the form of cylindrical segments and are joined using the submerged arc welding (SAW) process. Therefore, in this study, two 90-mm-thick hot-rolled S355 plates of 1300 mm width and 800 mm length each as shown in Fig. 1(b) were used for the SAW process to replicate the thick welded joints in wind turbine applications.

The initial bevel design of the joint is represented by the solid lines in Fig. 1(c), where one side of the joint shows the groove machined at an angle of $44° \pm 5°$, while the remaining section of the joint has a separation of less than 5 mm. The first step in the joining operation involved tack welding of the plates at locations marked in Fig. 1(c), followed by multi-pass welding of the grooved section involving 18 weld passes. In the next step, a second groove (similar to the first groove) was machined on the opposite face of the plates, as shown by the dotted lines in Fig. 1(c). Finally, the second groove was joined using multi-pass welding, with 25 weld passes to obtain a through thickness weld joint resembling the thick monopile weldments. EN ISO 14171A (EN 756): S3Si and EN ISO 14174: SA FB 1 55 AC H were used as solid wire electrode and flux, respectively, for the welding. Figure 1(d) shows the overall weldment with the weld passes outlined and numbered according to the order of deposition. The face marked as ''inner wall'' corresponds to the inner surface of the monopile cylinder and the ''outer wall'' corresponds to the outer surface of the monopile that is in direct contact with the seawater.

2.2 Specimens Design and Test Methods

A dog-bone specimen (with rectangular cross-sectional area) and a round bar specimen (with circular cross-sectional area) were machined for the *in situ* static and cyclic tests according to ASTM E8 (Ref 26) and ASTM E606 (Ref 27) standard as shown in Fig. 2(a) and (b), respectively. The specimens were extracted at the weld region such that the gauge section contained part of the WM, HAZ and the BM microstructure, as shown in Fig. 1(d). Both tests were performed at a strain rate of 10^{-4} s^{-1} using a 50 kN mechanical testing rig installed at the time-of-flight neutron diffractometer, ENGIN-X at ISIS Neutron and Muon Source, Rutherford Appleton Laboratory, UK. A schematic of the *in situ* neutron diffraction measurement setup is shown in Fig. 2(c), which shows the specimen loading axis oriented at 45° to the incident beam and the diffracted neutron detectors placed at $\pm$ 90° to the incident beam. The two detectors record the complete diffraction spectrum with different crystallographic planes contributing to the spectrum in the longitudinal (along the loading axis) and transverse directions (perpendicular to the loading axis). An extensometer with a gauge length of 12.5 mm was used for performing the cyclic test under the strain-controlled mode. Additionally, digital image correlation (DIC) technique was used in both static and cyclic tests to record the dissimilar material response at the WM, HAZ and BM regions of the weldment.

A stepped loading profile was applied in both tests with a 10 min hold time at each load step to perform the neutron diffraction measurements in the three regions, i.e., WM, HAZ and BM. At each point, using the Bragg's law (Eq 1) the *d*-spacing was measured by applying individual peak refinement from the whole diffraction spectrum (Fig. 2d) obtained from each region of the graded weldment. In order to calculate intergranular lattice strains for different crystallographic orientations, d_0 reference values were measured for the BM, HAZ and WM at a stress level of value close to zero (i.e., 5 MPa) and the lattice strains at different macro stress levels were calculated using Eq 2. The DIC strain maps were also captured in the overall gauge section during the hold time. The in situ (uniaxial) static load test was conducted at room temperature and maximum strain level of 6%. In this test, the sample was pulled in tension using the load-controlled mode for the first 5 measurement points at 5, 100, 200, 300 and 430 MPa, which fall within the elastic regime. For higher loads, the test was continued under strain-controlled mode to measure another 10 points in the plastic regime.

Similarly, the cyclic test was performed with the same methodology with a fully reversed strain amplitude of $\pm$ 3%. The loading steps for the cyclic load test is shown in Table 2. It is worth mentioning that the cyclic test was performed in load-controlled mode during the first 3 load steps where the applied stress is below the yield strength. The reason for selecting 430 MPa as the limit for the load-controlled step in the cyclic and static tests was based on the 0.2% proof stress value of S355G10+M reported for BM, HAZ and WM to be 455 MPa, 469 MPa and 477 MPa, respectively (Ref 12). The loading mode was switched to strain-controlled mode post yielding. A gauge volume of $2 \times 2 \times 2$ mm (Ref 3) was used in both

Table 1 Chemical composition (weight %) of the plate base metal and filler wire (ISO 14171-A) (Ref 12)

Element	Base metal	Wire	Element	Base metal	Wire
C	0.061	0.07-0.15	V	0.001	…
Si	0.28	0.15-0.4	Nb	0.022	…
Mn	1.58	1.3-1.85	As	0.003	…
Mo	0.006	0.15	Sn	0.001	…
Ni	0.342	0.15	Ti	0.003	…
Cr	0.034	0.15	B	0.0003	…
P	0.013	0.025	Sb	0.001	…
S	0.0007	0.025	Ca	0.0028	…
Cu	0.254	0.3	Bi	0.0001	…
N	0.0041	…	Al total	0.032	…

Single values represent the maximum permissible weight % for the element

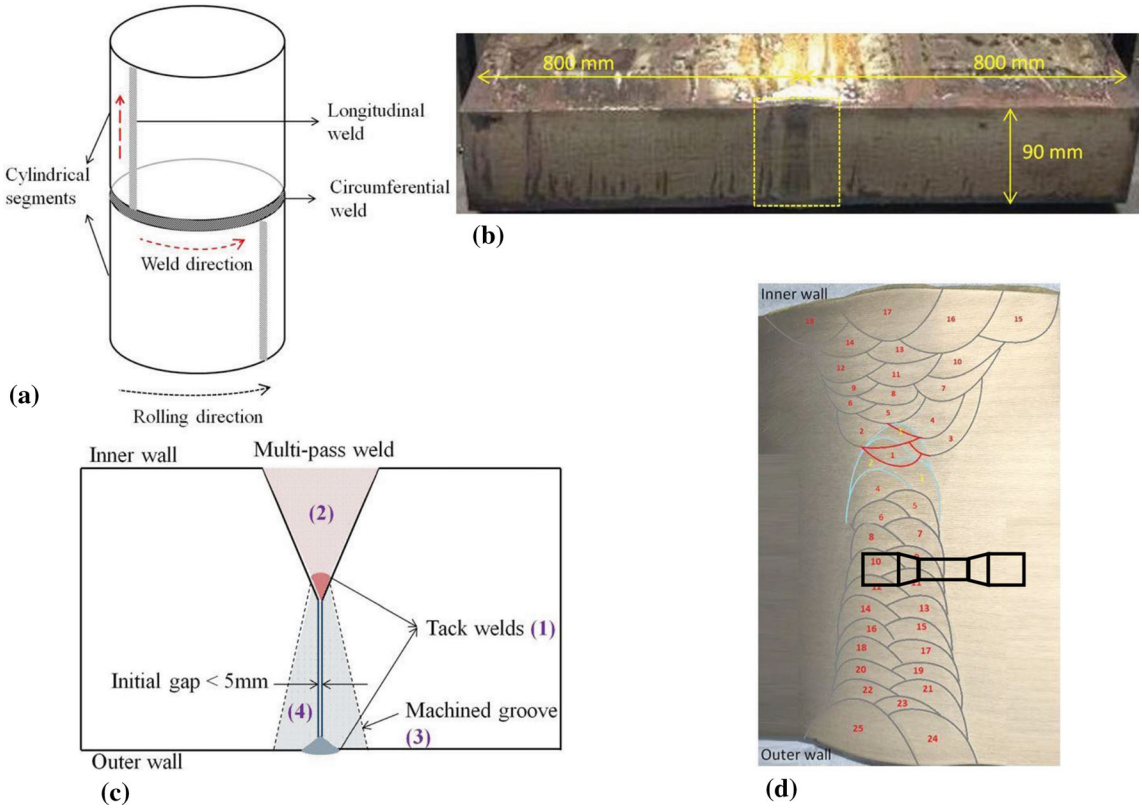

Fig. 1 (a) Schematic of weld configurations used in OWT monopile structure. Note: dashed arrows in red indicate welding direction and dashed arrow in black indicates the rolling direction, (b) hot-rolled S355 G10+M plate in as-welded condition, (c) weld joint configuration and welding order adopted to attain through thickness joint, (d) detailed view of the multi-pass weld joint highlighted in (b), with the overlapping weld regions marked by blue outlines and the remaining passes marked by grey lines. Specimen extraction location with respect to weld region is marked in black sketch

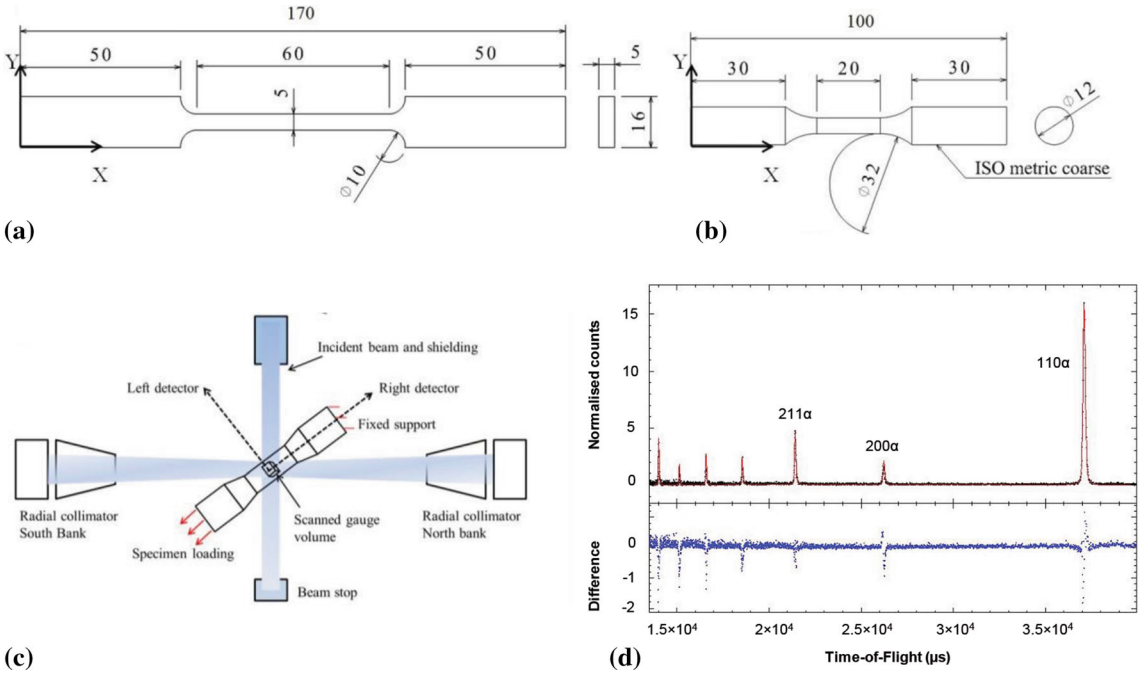

Fig. 2 Specimen geometry used for in situ: (a) tensile, (b) cyclic tests; (c) schematic of neutron diffraction measurement setup. Specimen was axially loaded along *x*-axis, therefore *X* and *Y* directions are referred as axial and lateral orientations, respectively, (d) neutron diffraction pattern obtained from the instrument

experiments, to ensure that enough number of grains are captured for each measurement.

$$n\lambda = 2d_{hkl}\sin\theta \quad \text{(Eq 1)}$$

$$\varepsilon_{hkl} = \frac{d_{hkl} - d_{0,hkl}}{d_{0,hkl}} \quad \text{(Eq 2)}$$

3. Hardness and Microstructural Analysis

3.1 Hardness Test Results

The OWT weldments often involve joining of thick sections which can be achieved by multi-pass welding. Deposition of the successive layers result in elastic, plastic, creep and viscous deformations of the previously deposited layer to undergo heat treatments above the tempering temperature of the material. Micro hardness value gives an indication of the phase distribution (ferrite or pearlite) in S355 at the measured location. Therefore, Vickers hardness measurement was taken on a cross-weld sample, without prior deformation, to study the distribution of hardness over the entire weld and the associated heat-affected region. Hardness measurements were made using Vickers micro hardness with a load of 100 g applied for 15 s to observe the hardness variations across different regions of the weld. The measurements were taken every 0.5 mm distance as shown in Fig. 3(a). The average value of micro hardness was found to be higher in the BM, i.e., 239.7 HV, as compared to 197 HV and 199 HV measured at the WM and HAZ, respectively.

3.2 Microstructural Analysis

A cross-weld sample was prepared for metallurgical analysis according to ASTM E3-11 (Ref 28). The sample was polished and etched using 2% Nital solution (2% HNO3 and 98% ethanol vol/vol) for 10 s to study the material microstructure. Following this, the grain size and distribution characteristics in the cross-weld metallography specimen were studied under optical and scanning electron microscope (SEM). The cross-weld sample was studied to understand the primary weld microstructure because the OWT structures are designed to be used in as-welded condition. Though the direction of heat flow is three dimensional due to the large thickness of the plate as compared to the weld size (Fig. 1d), the prior austenitic grain boundaries were observed to grow epitaxially from the fusion zone opposite to the direction of heat extraction as shown in Fig. 3(b). This is because the heat flow from the center of the weld to the periphery is more dominating as compared to the other directions.

The ferrite grain size variation in the three regions (WM, HAZ and BM) was measured using ImageJ software. The grain size was estimated by fitting each grain with an elliptical geometry and using the length of major diameter of the ellipse to represent the grain size distribution. Predictably, the average grain size in the WM was the smallest and those of HAZ and BM were comparable, with average grain size values of 2.9 ± 1.3 µm, 4.5 ± 0.8 µm and 4 ± 1.5 µm, respectively. Furthermore, optical image of WM in Fig. 4(a) reveals that it is predominantly composed of allotriomorphic ferrite and Widmanstätten ferrite phases. Multi-pass welding process causes remelting, solidification and heating cycles above the Ac_1 and Ac_3 in various degrees. This causes the deposited layers (or initial weld microstructure) to undergo further diffusion of interstitial and substitutional atoms above the austenisation temperature and change from columnar grain morphology to relatively equiaxed grains. These regions can be found adjacent to the weld pass boundaries. Therefore, parts of the WM microstructure adjacent to the weld pass boundaries were found to consist of equiaxed ferrite grains similar to the HAZ microstructure in Fig. 4(b). On the other hand, the BM microstructure was found to consist of significant amount of pro-eutectoid ferrite nucleated on grain boundaries (grain boundary ferrite) and protruded through grain body (Widmanstatten ferrite) (Fig. 4c) developed from the thermal cycle during manufacturing of the steel plates.

The etched sample was also examined using SEM to study the varying morphologies of ferrite phase in the WM, HAZ and BM. Parts of the WM exhibited acicular ferrite morphologies as shown in Fig. 5(a). Similarly, the SEM images of HAZ (Fig. 5b) and BM (Fig. 5c) showed detailed morphology of the ferrite grains, with clear indication of a normalized microstructure in the HAZ.

Table 2 Test plan used for the loading and unloading of *in situ* neutron diffraction measurement under fully reversed cyclic load application

Load step	Applied stress, MPa	Applied strain, %	Load step	Applied stress, MPa	Applied strain, %
1[a]	5	…	11	…	−2
2[a]	350	…	12	…	−3
3[a]	430	…	13	…	−2.5
4	…	2	14	…	−2
5	…	3	15	…	−1
6	…	2.5	16	…	0
7	…	2	17	…	1
8	…	1	18	…	2
9	…	0	19	…	3
10	…	−1			

[a]Load step 1–3 are load-controlled mode while the remaining steps are strain-controlled mode.

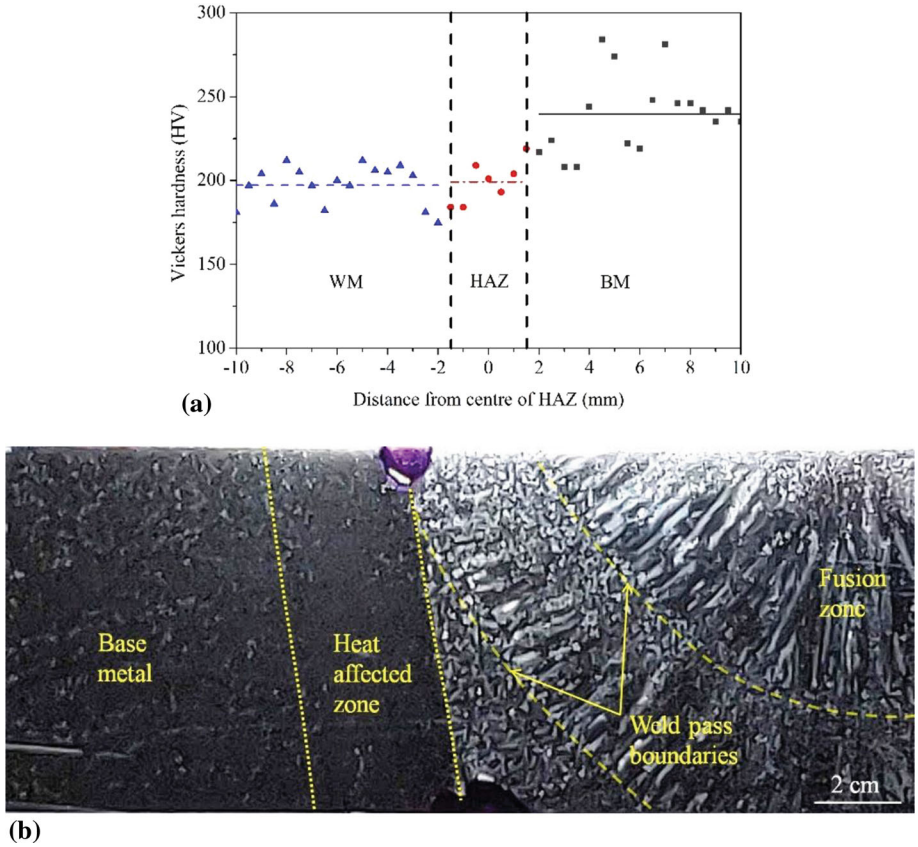

Fig. 3 (a) Average micro hardness values for the BM, HAZ and WM, with the HAZ considered as the '0' point. Please note that the width of HAZ was about 3mm, (b) Primary weld microstructure showing epitaxial grain growth in the fusion zone

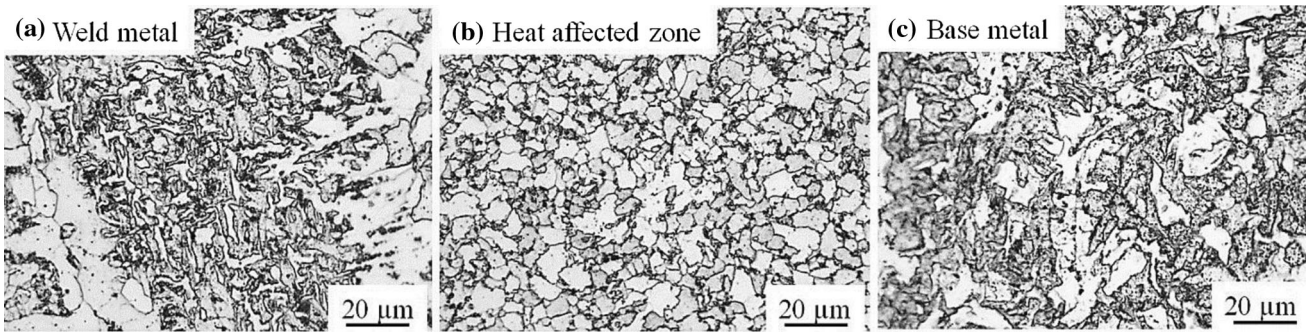

Fig. 4 Microstructural observations using optical microscopy for: (a) WM, (b) HAZ and (c) BM

4. Measurement of Lattice Strain Resulting from Tensile and Cyclic Loads

Cross-weld specimens manufactured using submerged arc welding may exhibit inferior tensile behavior compared to the BM due to the heterogeneous microstructure and weld defects (Ref 29). The use of in situ tensile loading approach revealed the differential material response (indicated by the unique diffraction peaks of individual hkl reflections) at the three distinct microstructural zones, namely WM, HAZ and BM. From the complete diffraction spectrum, individual peak analysis of {110}, {200} and {211} crystallographic planes was conducted. Additionally, the overall strain response (measured using an extensometer and DIC technique) was used to compare the crystallographic lattice strain response to the macro response of the cross-weld specimen. Lattice strain corresponds to the averaged strain response of a selected family of grains over a scanned volume of 8 mm (Ref 3), which is the gauge volume for this measurement. The lattice deformation behavior for the {110}, {200} and {211} families of crystallographic planes has been measured using in situ tensile and cyclic tests and the results are presented in the following sections.

4.1 In situ Tensile Test

The material response in the individual crystallographic planes were obtained from the *in situ* tensile test on the cross-weld specimen and presented in Fig. 6. The Young's modulus,

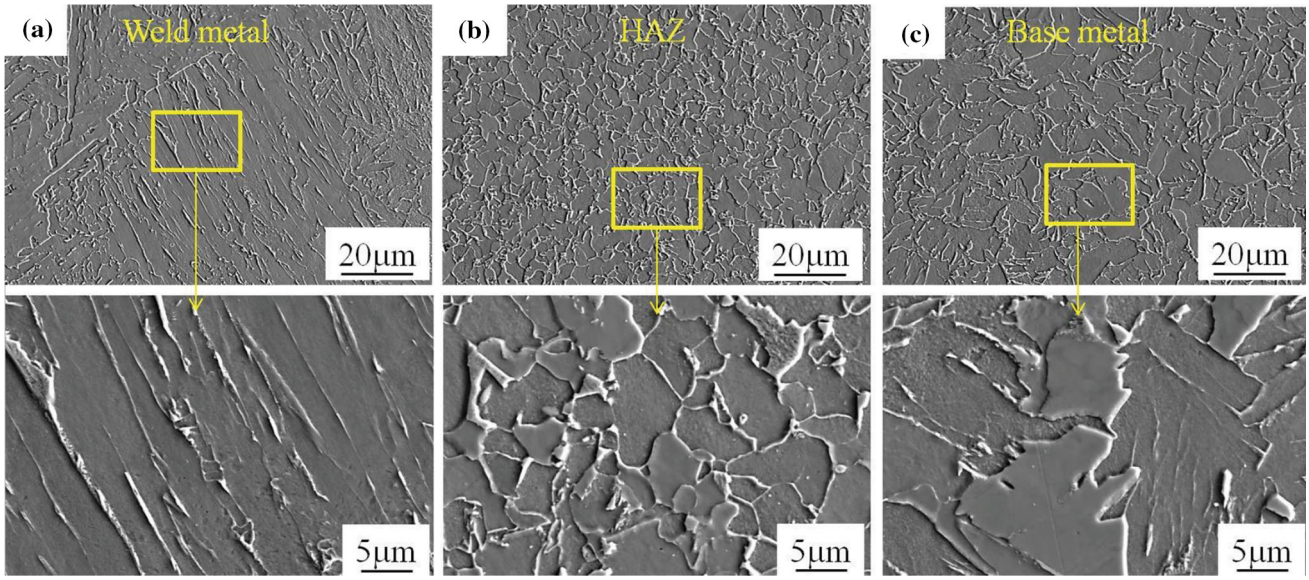

Fig. 5 Microstructure of S355 observed via electron microscopy at, (a) WM showing acicular ferrite, (b) HAZ, showing equiaxed ferrite and (c) BM

E, and Poisson's ratio, *v*, from these tests have been summarized in Table 3. Figure 6 and Table 3 shows the results obtained for three families of crystallographic planes (i.e., {110}, {200} and {211}) from the BM, HAZ and WM material microstructures. As seen in Fig. 6, within the elastic regime a linear relationship between the macroscopic stress and lattice strain was obtained for both axial (i.e., along *X*-axis in Fig. 2a) and lateral (i.e., along *Y*-axis in Fig. 2a) directions. The crystallographic response observed within a specific microstructure was anisotropic and dependent upon the examined crystallographic plane as shown in Table 3. It is worth mentioning that the chosen crystallographic planes represent the most commonly studied planes for ferritic steels (Ref 20) and therefore can be considered to represent the important aspects of the bulk mechanical response of the material. The dependence of elastic deformation on the crystallographic orientation will lead to intergranular stress accumulation during loading. Furthermore, the plastic anisotropy assists the accumulation of intergranular stresses due to the differential straining of the neighboring grains.

The stiffness of the crystallographic orientations {110}, {200} and {211} in the axial direction was close to the macro Young's modulus of S355 and had a value of 207 GPa for the cross-weld specimen. DIC measurements showed the three regions of the cross-weld specimen, namely the BM, HAZ and WM exhibited varying stiffness values in respective orientations. However, the response of BM and HAZ was comparable for all three orientations in the axial loading direction while the WM resulted in the lowest stiffness and the highest deviation from the overall stiffness. Higher degree of anisotropy observed in the WM can be attributed to the dendritic grain morphology and different chemical composition as a result of use of filler wire. On the application of tensile load, the anisotropic material behavior leads to the development of intergranular stresses at interfaces of different crystallographic orientations which causes the variation in the lattice strengths depending on the weld region (Ref 20). Particularly, the {110} and {200} orientations result in 40 to 50% lower stiffness which indicates that the interface at the WM and HAZ would be prone to crack initiation, more so in case of strong {110} or {200} texture. The stiffness of {211} orientation was closest to the gross material response, irrespective of the type of the material microstructure. On the contrary, the lateral stiffness values did not show consistent trends in the three lattice orientations as well as in the different weld microstructures (BM, WM and HAZ) except that the value was negative in all the cases due to the Poisson's contraction. This behavior is due to the heterogeneous elastic contraction resulting in significantly lower lattice strain values in the {211} crystallographic orientation.

Differential strain accumulation results in development of the complex stresses to maintain isochoric plastic deformation as shown in the lattice strain response at HAZ region in Fig. 6(d). Similar observations have been made for the {200} reflection in austenitic and ferritic steels as reported in (Ref 20, 21). Figure 6(d) also shows that the lattice response of the {110} and {211} planes remain fairly linear even in the plastic regime for the lateral direction, thereby indicating that the planes undergo late yielding. The {200} orientation on the other hand becomes approximately vertical due to the development of tensile internal stress.

Studies related to conversion of strain to stress are inherently complex due to the 36 independent components of the elastic stiffness tensor. Moreover, the errors involved with strain measurement makes it challenging to calculate the true stresses on the parts. On the application of load, the anisotropic deformation of individual lattice planes gives rise to intergranular stresses. In bcc steels such as S355, the families {110} and {211} are the planes which are weakly affected by the intergranular strains, while {200} shows the maximum impact (Ref 21). However, most engineering applications can be computed using an isotropic assumption, which leaves the elastic stiffness tensor with two independent variables, namely the Young's modulus and Poisson's ratio. Reuss (Eq 3-4) and Kröner models (Ref 30) are widely used for the prediction of elastic response of fcc and bcc materials based on the hkl-specific response (lattice deformations) measured by neutron diffraction technique. Calculation of the hkl-specific elastic modulus and Poisson's ratio according to Kröner's model is

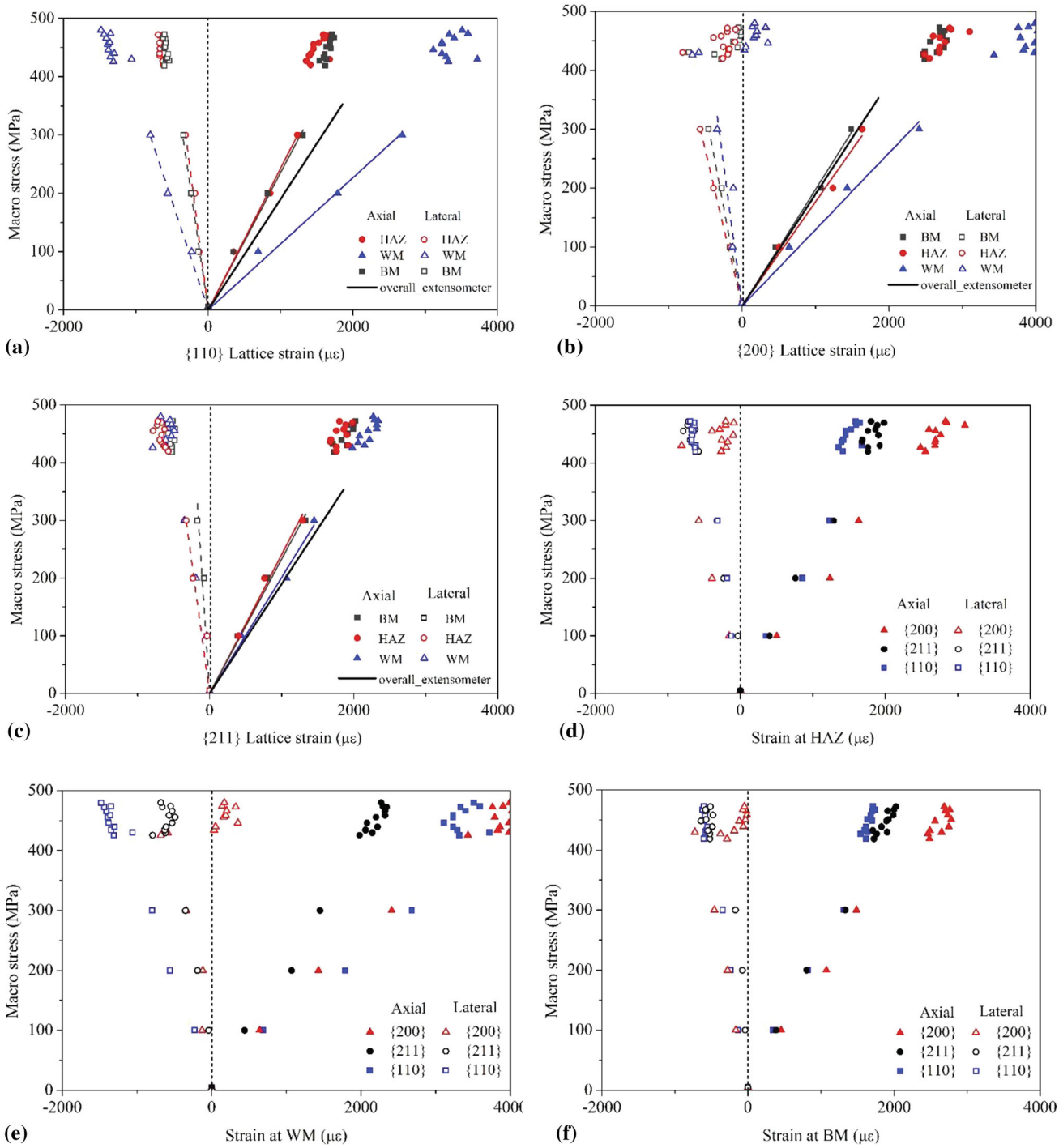

Fig. 6 Comparison of lattice strain response for BM, HAZ and WM under static loading for: (a) {110}, (b) {200} and (c) {211} crystallographic orientations; comparison of strain response for {110}, {200} and {211} crystallographic orientations at (d) HAZ, (e) WM and (f) BM

relatively complex and the detailed procedure can be found elsewhere (Ref 31).

$$E^{R}_{hkl} = \frac{1}{S_{11} - 2S_0 A_{hkl}} \quad \text{(Eq 3)}$$

$$v^{R}_{hkl} = \frac{S_{12} + S_0 A_{hkl}}{S_{11} - 2S_0 A_{hkl}} \quad \text{(Eq 4)}$$

where E^{R}_{hkl} is the elastic Young's modulus specific for the hkl orientation, v^{R}_{hkl} the Poisson's ratio which gives the ratio of the lattice strains perpendicular and parallel to the loading direction. S_{11} and S_{12} are elastic compliance constants and the respective values for *bcc* ferrite (base metal) are given as 0.8×10^{-2} GPa^{-1} and -0.28×10^{-2} GPa^{-1} (Ref 30). S_0 expresses the degree of anisotropy and is equal to 2.51 and A_{hkl} gives the orientation (hkl) dependency of elastic Young's modulus and is computed for each lattice using Eq 5.

$$A_{hkl} = \frac{h^2k^2 + k^2l^2 + l^2h^2}{h^2 + k^2 + l^2} \quad \text{(Eq 5)}$$

Figure 7 (a) compares the E_{hkl} values predicted using Reuss and Kröner models to the experimental results obtained in this study for S355 in the axial direction. For BM, the error in prediction was the greatest for {200} orientation, with Kröner model being less conservative and resulting in 12.4% lower prediction as compared to Reuss model, where the prediction was 36.8% lower. Comparison of the lattice specific Poisson's ratio of the BM with the predictions of the aforementioned models rendered reasonably accurate results for {110} and {200} orientations as shown in Fig. 7(b), while the {211} orientation showed significant overprediction. Also included in Fig. 7 is the results obtained for the HAZ and WM material microstructures. As seen in this figure, both models could successfully predict the Young's modulus and Poisson's ratio for HAZ microstructure, with Kröner model giving better prediction such that the maximum error was limited to 7% (corresponding to {110} orientation). On the contrary, Reuss model predictions were more accurate (error for E was 4% and v was 17%) for the WM microstructure, except in the {110} orientation for the Young's modulus and the {200} orientation for the Poisson's ratio. Besides, Kröner model also failed to predict the Young's modulus and Poisson's ratio values for the {110} and {200} orientations, respectively, for the WM.

4.2 In situ Cyclic Test

The material response of the three crystallographic planes (i.e., {110}, {200} and {211}) was studied under *in situ* cyclic loading conditions as described earlier in section 2.2, and the experimental measurements in the loading direction are presented in Fig. 8. The applied load level was controlled by the macroscopic strain in the specimen gauge section, except for the first three load steps, which were applied in load-controlled method (refer to Table 2). Figure 8(a) shows the lattice strain response of the {110} crystallographic orientation for the specific microstructural zones, i.e., WM, HAZ and BM, with respect to the applied macroscopic strain of ± 3%. Similar results for the {200} and {211} orientations are shown in Fig. 8(b) and (c), respectively. Significant differences were observed between the lattice strain loops of the three statistically well-defined hkl reflections. The {200} crystallographic orientation displayed higher plastic strains thereby generating greater intergranular strain misfits as shown in Fig. 8(b). As discussed in section 4.1, the variation in the intergranular strain of individual hkl reflections originates from the fact that while some grain families (such as {200} in this study, Fig. 8b) undergo yielding, the others continue to exhibit elastic behavior for the same applied macroscopic strain.

Another factor affecting the lattice strain loops is the material microstructure. Figure 8 (d-f) shows the microstructure specific anisotropic response of the individual crystallographic orientations. It can be observed that the {200} orientation (Fig. 8b) and WM microstructure (Fig. 8e) exhibited the least load carrying capacity as compared to the other crystallographic orientations and material microstructures studied. Another interesting result observed from the lattice deformation is the reduction in material stiffness in the second cycle. This behavior was noticed in all studied crystallographic orientations. This phenomenon indicates that S355 undergoes cyclic softening, i.e., the dislocation substructure rearranges to give reduced resistance to subsequent load cycles.

Table 3 Mechanical properties for dominant lattice planes in S355 measured using neutron diffraction technique

	BM			HAZ			WM		
Lattice plane	**{110}**	**{200}**	**{211}**	**{110}**	**{200}**	**{211}**	**{110}**	**{200}**	**{211}**
E_{xx} (GPa)	235.4 ± 7.8	197.9 ± 5.3	233.1 ± 7.1	242.8 ± 6.2	177.1 ± 6.7	240.9 ± 7.5	113.3 ± 3.9	129.8 ± 5.2	201.4 ± 6.5
v	0.278	0.299	0.121	0.252	0.337	0.262	0.304	0.137	0.219

E_{xx} denotes the axial elastic Young's modulus and v the Poisson's ratio

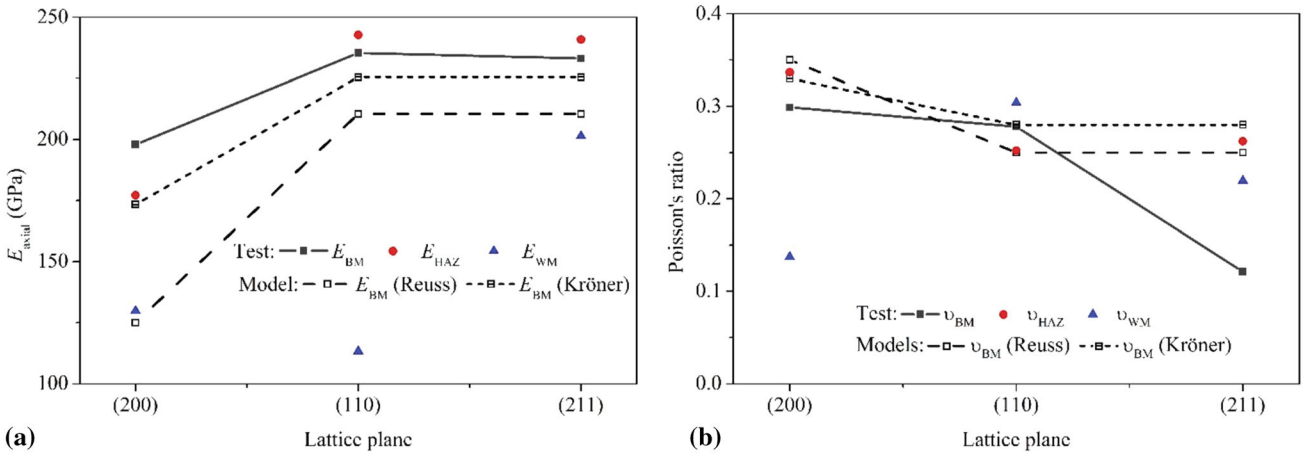

Fig. 7 Variation in (a) Young's modulus and (b) Poisson's ratio with lattice orientations

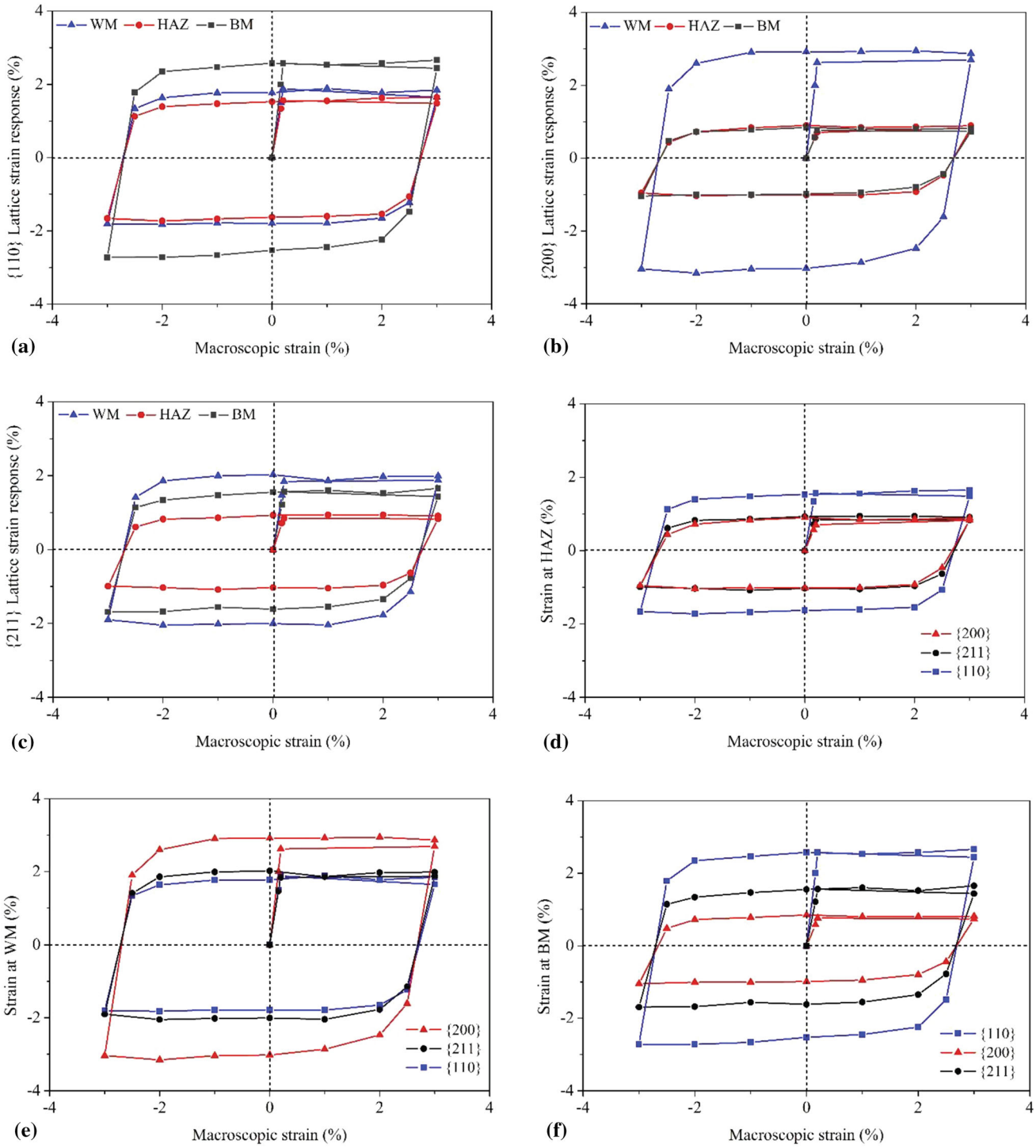

Fig. 8 Lattice strain response at the BM, HAZ and WM under cyclic loading: (a) {110}, (b) {200} and (c) {211} orientations; comparison of the strain response of the lattice planes {110}, {200} and {211} at: (d) HAZ, (e) WM and (f) BM

4.3 Electron Backscatter Diffraction (EBSD) Analysis

The specimens subjected to 6% uniaxial tensile load and ± 3% uniaxial cyclic load, were studied using EBSD technique to understand the grain orientation distribution on a plane parallel to the loading axis. An additional EBSD sample was extracted from the welded plate which was used for the tensile and cyclic load specimen extraction. Therefore, the third sample has no known prior loading history and should ideally represent the initial material microstructure. Figure 9 represents a typical EBSD map of the material after subjecting to the three specified loading conditions (i.e., no load, tensile load 6% and cyclic load ± 3%). Figure 9(a) gives the intrinsic material microstructure at the junction between the WM and HAZ. Grain sizes ranging approximately between 2 and 10 µm were found on either side of the WM/HAZ interface. The grain orientation distribution was near random in nature.

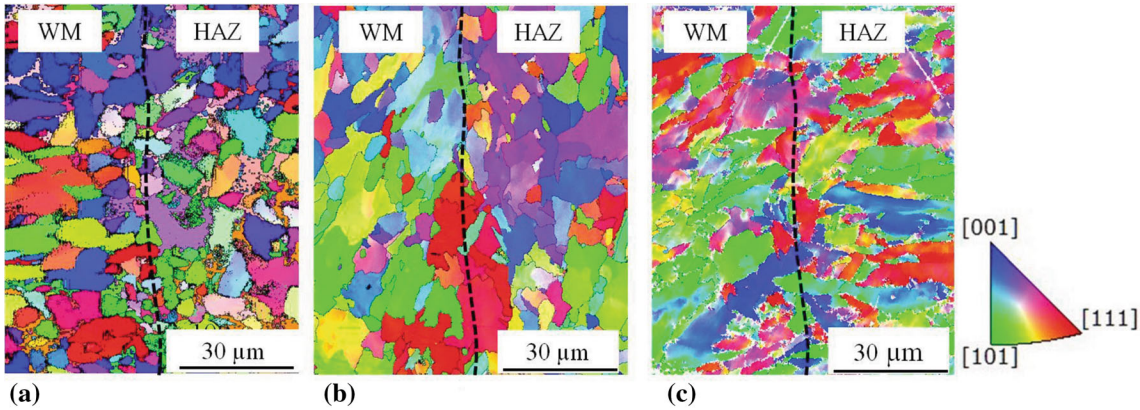

Fig. 9 EBSD maps taken at the weld metal and heat-affected zone (WM/HAZ) interface of specimen with: (a) no prior loading history, (b) 6% tensile load history and (c) ± 3% cyclic strain history. The key is given in terms of inverse pole map in the bottom right of (c).

Figure 9(b) and (c) exhibited noticeable similarity in the morphology of the grains, which were pulled along the loading direction (loading direction was perpendicular to the WM/HAZ interface). Nevertheless, the changes in the grain morphology were far more eminent in the specimen with cyclic loading history. This is because, under cyclic loading condition, the crystallographic orientation of the individual grains will control the lattice strain and lead to dislocation pileups at the high-angle grain boundaries. Further, it is known that {110} <111> slip system is a preferred slip system in the bcc crystal lattice, thereby explaining the marked rise in the grains orientated toward {101} direction in the specimens with tensile and cyclic loading history.

5. Conclusion

In situ neutron diffraction measurements were conducted on S355 G10+M steel cross-weld specimens under static and cyclic loading conditions to study and compare the evolution of internal stresses in the {110}, {200} and {211} crystallographic planes in the three distinct regions of the weld. Following this, hardness measurement, microstructural analysis and texture strength analysis were performed to correlate the mechanical response to the material microstructure at the weld metal (WM), heat-affected zone (HAZ) and base metal (BM) for the cross-weld specimen. The main findings of this study are summarized below:

1. Lattice strains were found to be dependent on crystallographic orientation and material microstructure for the cross-weld specimens. While the {200} crystallographic orientation was found to be more compliant (more so in case of WM microstructure), and the {211} crystallographic orientation exhibited the maximum stiffness (particularly in HAZ microstructure) under both static and cyclic loading conditions.
2. The hkl-specific response predicted using Reuss and Kröner model were found to agree well with experimental values obtained for the HAZ material microstructure for all the orientations, however, discrepancies in the Poisson's ratio for {211} crystallographic orientation in the BM microstructure has been observed between the values obtained from these models and the experiments. The test results showed that the heterogeneous elastic deformation in the respective crystallographic planes resulted in the observed mismatch.
3. The tensile test results showed that the {110} and {200} orientations result in 40% to 50% lower stiffness which indicates that the interface at the WM and HAZ would be prone to crack initiation, more so in case of strong {110} or {200} texture.
4. The cyclic test results revealed that maximum mismatch between the elastic–plastic strain energy accumulations occur at the interface between the WM and HAZ. This raises concerns from fatigue crack initiation perspective.

6. Materials and methods

In situ neutron diffraction measurements were taken on cross-weld S355 test samples at room temperature to monitor the evolution of intergranular strains under static and cyclic loading conditions.

Acknowledgment

The authors would like to acknowledge Dr Anaïs Jacob and Dr Victor Igwemezie for their contribution toward the specimen preparation. This work was supported by grant EP/L016303/1 for Cranfield, Oxford and Strathclyde Universities, Centre for Doctoral Training in Renewable Energy Marine Structures—REMS from the UK Engineering and Physical Sciences Research Council (EPSRC).

Data Availability

The datasets generated during and/or analyzed during the current study are available from the corresponding author on request.

References

1. C. Giorgio, A. Ho and I. Pineda, Wind Energy Scenarios for 2030. Tech. Rep. (2015)
2. V. Igwemezie, A. Mehmanparast and A. Kolios, Current Trend in Offshore Wind Energy Sector And Material Requirements for Fatigue Resistance Improvement in Large Wind Turbine Support Structures–A Review, *Renew. Sustain. Energy Rev.*, 2019, **101**, p 181–196.
3. D.N. Veritas, Fatigue Design of Offshore Steel Structures. Tech. Rep. (2011)
4. A. Mehmanparast, F. Brennan and I. Tavares, Fatigue Crack Growth Rates for Offshore Wind Monopile Weldments in Air and Seawater: SLIC Inter-Laboratory Test Results, *Mater. Des.*, 2017, **114**, p 494–504.
5. R. Biswal and A. Mehmanparast, Fatigue Damage Analysis of Offshore Wind Turbine Monopile Weldments, *Procedia Struct. Integr.*, 2019, **17**, p 643–650.
6. A. Jacob, A. Mehmanparast, R. D'Urzo and J. Kelleher, Experimental and Numerical Investigation of Residual Stress Effects on Fatigue Crack Growth Behaviour of S355 Steel Weldments, *Int. J. Fatigue*, 2019, **128**, p 105196.
7. D.F. Li, C.M. Davies, S.Y. Zhang, C. Dickinson and N.P. O'Dowd, The Effect of Prior Deformation on Subsequent Microplasticity and Damage Evolution in an Austenitic Stainless Steel at Elevated Temperature, *Acta Mater.*, 2013, **61**(10), p 3575–3584.
8. Y. Wan, W. Jiang, M. Song et al., Distribution and Formation Mechanism of Residual Stress in Duplex Stainless Steel Weld Joint by Neutron Diffraction and Electron Backscatter Diffraction, *Mater. Des.*, 2019, **181**, p 108086.
9. J. Hu and A.C. Cocks, A Multi-Scale Self-Consistent Model Describing the Lattice Deformation in Austenitic Stainless Steels, *Int. J. Solids Struct.*, 2016, **78**, p 21–37.
10. V. Igwemezie, A. Mehmanparast and A. Kolios, Materials Selection for XL Wind Turbine Support Structures: A Corrosion-Fatigue Perspective, *Marine Struct.*, 2018, **61**, p 381–397.
11. V. Igwemezie, P. Dirisu and A. Mehmanparast, Critical Assessment of the Fatigue Crack Growth Rate Sensitivity to Material Microstructure in Ferrite-Pearlite Steels in Air and Marine Environment, *Mater. Sci. Eng. A*, 2019, **754**, p 750–765.
12. A. Jacob, J. Oliveira, A. Mehmanparast, F. Hosseinzadeh, J. Kelleher and F. Berto, Residual Stress Measurements in Offshore Wind Monopile Weldments Using Neutron Diffraction Technique and Contour Method, *Theor. Appl. Fract. Mech.*, 2018, **96**, p 418–427.
13. G. Sun, Y. Chen, S. Chen and D. Shang, Fatigue Modeling and Life Prediction for Friction Stir Welded Joint Based on Microstructure and Mechanical Characterization, *Int. J. Fatigue*, 2017, **98**, p 131–141.
14. X. Liu, K.F. Chung, M. Huang, G. Wang and D.A. Nethercot, Thermomechanical Parametric Studies on Residual Stresses in S355 and S690 Welded H-Sections, *J. Constr. Steel Res.*, 2019, **160**, p 387–401.
15. C. Gu, J. Lian, Y. Bao, Q. Xie and S. Münstermann, Microstructure-Based Fatigue Modelling with Residual Stresses: Prediction of the Fatigue Life for Various Inclusion Sizes, *Int. J. Fatigue*, 2019, **129**, p 105158.
16. R. Voothaluru, V. Bedekar, Q. Xie, A.D. Stoica, R.S. Hyde and K. An, In-situ neutron diffraction and crystal plasticity finite element modeling to study the kinematic stability of retained austenite in bearing steels, *Mater. Sci. Eng. A*, 2018, **711**, p 579–587.
17. R.W. Hertzberg, *Deformation and Fracture Mechanics of Engineering Materials*, 4th ed. Wiley, New Jersey, 1996
18. T. Yamashita, S. Morooka, S. Harjo, T. Kawasaki, N. Koga and O. Umezawa, Role of Retained Austenite in Low Alloy Steel at Low Temperature Monitored by Neutron Diffraction, *Scr. Mater.*, 2020, **177**, p 6–10.
19. R. Pokharel, A. Patra, D.W. Brown, B. Clausen, S.C. Vogel and G.T. Gray, An Analysis of Phase Stresses in Additively Manufactured 304L Stainless Steel using Neutron Diffraction Measurements and Crystal Plasticity Finite Element Simulations, *Int. J. Plast.*, 2019, **121**, p 201–217.
20. E.C. Oliver, M.R. Daymond and P.J. Withers, Interphase and Intergranular Stress Generation in Carbon Steels, *Acta Mater.*, 2004, **52**(7), p 1937–1951.
21. A.A. Mamun, R.J. Moat, J. Kelleher and P.J. Bouchard, The Effect of Cyclic-Loading Generated Intergranular Strains on the Creep Deformation of a Polycrystalline Material, *Materialia*, 2019, **7**, p 100385.
22. A.A. Mamun, R.J. Moat, J. Kelleher and P.J. Bouchard, Origin of the Bauschinger effect in a polycrystalline material, *Mater. Sci. Eng. A*, 2017, **707**, p 576–584.
23. W. Woo, J. Kim, E.Y. Kim, S.H. Choi, V. Em and D.S. Hussey, Multi-Scale Analyses of Constituent Phases in a Trip-Assisted Duplex Stainless Steel by Electron Backscatter Diffraction, in situ Neutron Diffraction, and Energy Selective Neutron Imaging, *Scr. Mater.*, 2019, **158**, p 105–109.
24. Y. Wang, T. Ohnuki, Y. Tomota, S. Harjo and T. Ohmura, Multi-Scaled Heterogeneous Deformation Behavior of Pearlite Steel Studied by in situ Neutron Diffraction, *Scr. Mater.*, 2017, **140**, p 45–49.
25. Y. Wang, Y. Tomota, S. Harjo, W. Gong and T. Ohmura, In-situ Neutron Diffraction During Tension-Compression Cyclic Deformation of a Pearlite Steel, *Mater. Sci. Eng. A*, 2016, **676**, p 522–530.
26. ASTM E8, ASTM E8/E8M standard test methods for tension testing of metallic materials 1, *Annu. B. ASTM Stand.*, 2010, **4**, p 1–27.
27. T. Modulus, C. Modulus and S. Rates, Strain-Controlled Fatigue Testing 1, *ASTM Stand.*, 2013, **E606**(92), p 1–16.
28. ASTM International, ASTM E3.34776 Stardard Guide for Preparation of Metallographic Specimens, *ASTM Stand.*, 2017, **11**, p 1–17.
29. S.R. Nathan, V. Balasubramanian, S. Malarvizhi and A.G. Rao, Effect of Welding Processes on Mechanical and Microstructural Characteristics of High Strength Low Alloy Naval Grade Steel Joints, *Def. Technol.*, 2015, **11**(3), p 308–317.
30. M. Hutchings, P.J. Withers, T. Holden and T. Lorentzen, *Introduction to the Characterization of Residual Stress by Neutron Diffraction*, 1st ed. Taylor & Francis group, UK, 2005
31. E. Kröner, Zur Plastischen Verformung des Vielkristalls, *Acta Metall.*, 1961, **9**, p 155–161.